frontiers | Frontiers in Earth Science

TYPE Original Research
PUBLISHED 11 July 2023
DOI 10.3389/feart.2023.1128827

OPEN ACCESS

EDITED BY
Hans-Balder Havenith,
University of Liège, Belgium

REVIEWED BY
Mircea Radulian,
National Institute for Earth Physics, Romania
Nimesh Chettri,
Royal University of Bhutan, Bhutan

*CORRESPONDENCE
Zhishuang Xu,
xzs0610@seis.ac.cn

RECEIVED 21 December 2022
ACCEPTED 28 June 2023
PUBLISHED 11 July 2023

CITATION
Xu Z, Liu J, Yalikun A, Li X, Ren J and Wen X (2023), Determination of the major axis direction and macroseismic epicenter of the assessed intensity map based on relocated aftershock sequences.
Front. Earth Sci. 11:1128827.
doi: 10.3389/feart.2023.1128827

Determination of the major axis direction and macroseismic epicenter of the assessed intensity map based on relocated aftershock sequences

Zhishuang Xu[1]*, Jie Liu[1], Alimujiang Yalikun[2], Xiaoli Li[1], Jing Ren[1] and Xintao Wen[1]

[1]China Earthquake Networks Center, Beijing, China, [2]Earthquake Administration of Xinjiang Uygur Autonomous Region, Urumqi, China

The rapid assessment of an intensity map following a strong earthquake forms the foundation for risk assessment and emergency response in Chinese mainland. The determination of the major axis direction in the assessed intensity map depends on various factors, including nearby active faults, instrumental intensities, and the distribution of aftershocks. To evaluate the effectiveness of promptly determining the major axis direction based on early aftershock distribution, we relocated and analyzed aftershock sequences occurring within 2 h of eighteen aftershock-rich earthquakes with a magnitude of $Ms \geq 6.0$ in Chinese mainland from 2012 to 2021. HypoDD was used for relocation, and the standard deviational ellipse fitting technique was employed for analysis. Comparing the aftershock ellipses resulting from our analysis with the macroseismic intensity maps obtained from field surveys reveals a high level of agreement, with an average difference of approximately 9° in the major axis directions of the aftershock ellipses and the meizoseismal zones. For the majority of earthquakes, regardless of focal mechanisms, the lengths of the major axes of the aftershock ellipses closely correspond to the intensity VIII scale. Additionally, the spatial distribution of aftershocks aids in distinguishing the seismogenic fault from the two fault planes with distinctly different dips as indicated by the focal mechanism solution. Moreover, the distance between the aftershock center and the macroseismic epicenter systematically increases as the dip decreases. These findings hold significant scientific value as they contribute to the prompt determination of assessed intensity maps and provide effective guidance for earthquake emergency response.

KEYWORDS

assessed intensity map, aftershock sequences, major axis direction, macroseismic epicenter, earthquake emergency response

Introduction

China is among the countries with a high level of seismic activity worldwide, particularly in the North-South seismic belt and the Tianshan seismic belt, which are recognized regions with above-average seismicity. It is common for these areas to experience one or two large earthquakes per year, often accompanied by numerous aftershocks near the hypocenters of

these main earthquakes. Between 2012 and 2021, over 20 earthquakes with surface wave magnitudes (*Ms*) exceeding 6.0 and highest macroseismic intensities equal to or greater than VIII were recorded in Chinese mainland. Out of these, 18 were found to have significant aftershock activity. Among the 18 earthquakes, nine exhibited dip-slip or thrust mechanisms with some strike-slip components, while the others were either strike-slip or predominantly strike-slip with some thrust components.

The assessment of seismic intensity is typically performed within minutes of the mainshock using either seismic intensity attenuation equations or ground-motion prediction equations (Wang et al., 2000; Bakun and Scotti, 2006; Allen et al., 2012; Sun et al., 2014; Cilia et al., 2017; Kiani et al., 2019; Ferrario et al., 2020). The major axis direction of the assessed intensity map is determined by considering various factors, including nearby active faults, ShakeMaps, aftershock sequences, instrumental intensities, focal mechanisms, and rupture processes (Chen et al., 2018; Xu et al., 2020; Xu et al., 2022). The results of this rapid assessment, especially the identification of high-intensity areas (around VIII or higher), play a crucial role in guiding earthquake emergency responses. Subsequently, a field survey of macroseismic effects is conducted on the same day as the mainshock, based on the assessed intensity map. The actual intensity map, which incorporates the cumulative effects of the earthquake sequence, is officially determined and published by the Ministry of Emergency Management of the People's Republic of China (Yuan, 2008).

The major axis direction and location of the macroseismic epicenter in the assessed intensity map have significant implications for loss assessments. Both the assessed and actual intensity maps generally exhibit elongated intensity contours parallel to the rupture plane, with the exception of nearly circular contours for intensity VI. Discrepancies exist in the major axis directions of the assessed and actual intensity maps, as well as in the locations of macroseismically and instrumentally derived epicenters in some cases. The assessed intensity maps not only assist decision-makers in organizing emergency rescue efforts and formulating recovery strategies but also serve as valuable resources for further seismic studies, including the exploration of empirical relationships between macroseismic intensities and epicentral distances (Sun et al., 2014; Vannucci et al., 2021). Therefore, improving the assessment of intensity direction is a challenging issue that requires attention and resolution.

The aftershock sequences following large shallow earthquakes, lasting several months and extending over dozens to hundreds of kilometers, can help determine the seismogenic fault and the major axis direction of the intensity map (Kisslinger and Jones, 1991; Cai et al., 2023). Studies have also found correlations between ground motions of the main shock and aftershocks, with overall motions influencing building destruction and macroseismic intensity distribution (Zhang et al., 2019; Li et al., 2022; Tesfamariam and Goda, 2022). Precise relocations of large earthquake sequences have been used to estimate fault geometry, rupture dimensions, and possible intensity distribution (e.g., Astiz et al., 2000; Henry and Das, 2001; Neo et al., 2020; Xu et al., 2020). In dip-slip earthquakes, aftershocks, highest shaking, and high intensities primarily occur in the hanging wall of the seismic fault, known as the hanging wall effect (Lekkas, 2010; Wang et al., 2010; Galli et al., 2017; Xu et al., 2020). Similarly, in strike-slip earthquakes, aftershocks are not symmetrically distributed along the fault but concentrate on one side (Astiz et al., 2000). Various methods have been proposed to study aftershock distribution, including linear distribution, two-dimensional Gaussian distribution, and directional distribution (Kagan, 2002; Matumoto and Latham, 1973; Xu et al., 2020). The trends in aftershock activity align closely with fault lines, and projecting aftershocks onto a vertical plane perpendicular to these trends aids in defining fault dips and lengths (Matumoto and Latham, 1973; Xu et al., 2020). Statistical analyses have indicated that the size of aftershock distribution primarily depends on the magnitude of the mainshock, rather than the focal mechanism (Kagan, 2002; Jiang et al., 2007), although fault width imposes certain limitations on dip-slip earthquakes (Henry and Das, 2001).

The main objective of this article is to investigate the relationships between macroseismic intensity maps and relocated aftershock sequences of large earthquakes in Chinese mainland over the past decade, particularly focusing on major axis directions and macroseismic epicenters. Furthermore, the study aims to discuss the implications of spatial aftershock distribution for intensity assessment. The findings of this research provide a method for promptly assessing the major axis direction and macroseismic epicenter of intensity maps, effectively guiding emergency rescue operations following large earthquakes.

Data and method

Data selection

In the past 10 years, Chinese mainland has experienced more than 20 earthquakes with a magnitude $M_S \geq 6.0$. Among these, 18 cases exhibited a high occurrence of aftershocks, with over 40 aftershocks recorded within 2 h after the mainshock. This study focuses on analyzing the aftershock sequences of these 18 earthquakes, as shown in Table 1; Figure 1. The focal mechanisms were obtained from the Global Centroid Moment Tensor Project (GCMT) (Dziewonski et al., 1981; Ekström et al., 2012), except for the M_S 6.0 Changning, Sichuan earthquake on 17 June 2019, which was taken from Xu et al. (2020). The intensity maps used in the study were obtained from field surveys conducted and released by the China Earthquake Administration, Ministry of Emergency Management of the People's Republic of China (refer to Supplementary Table S1 for details). The magnitudes of the earthquakes analyzed ranged from M_S 6.0 to 7.4 (moment magnitude M_W 5.7–7.4, as provided by the global GCMT).

Xu et al. (2020) previously investigated the aftershock distributions for various time intervals following the mainshock (0.5 h, 1 h, 2 h, and 3 h, up to 24 h). The results of the 2-h aftershock distributions were found to be consistent with the majority of the earthquakes studied here. Considering the necessity of rapid seismic assessment and emergency guidance, the 2-h aftershock distribution was selected as the preferred measure for the highly affected area in this study. The number of aftershocks recorded by the China Earthquake Networks Center (CENC), China Earthquake Administration, ranged from approximately 40–200 during the 2-h interval. In the case of earthquakes with significant foreshocks, such as the M_S 6.4 Yangbi, Yunnan earthquake on 21 May 2021, and the M_S 6.4 Jiashi, Xinjiang earthquake on 19 January 2020, the foreshocks were also included in the analysis.

TABLE 1 Parameters of studied earthquakes in Chinese mainland (2012–2021).

No.	Date (mm/dd/yyyy)	Location	M_S	M_W	Focal mechanism	Depth (km)	I_{max}
1	06/30/2012	Xinyuan, Xinjiang	6.6	6.3	strike with slight thrust	7	VIII
2	04/20/2013	Lushan, Sichuan	7.0	6.6	dip-slip	13	IX
3	07/22/2013	Minxian, Gansu	6.6	6.0	thrust with minor strike	20	VIII
4	05/30/2014	Yingjiang, Yunnan	6.1	5.9	strike-slip	12	VIII
5	08/03/2014	Ludian, Yunnan	6.5	6.2	strike-slip	10	IX
6	10/07/2014	Jinggu, Yunnan	6.6	6.1	strike-slip	10	VIII
7	11/22/2014	Kangding, Sichuan	6.3	6.1	strike-slip	20	VIII
8	07/03/2015	Pishan, Xinjiang	6.5	6.4	dip-slip	10	VIII
9	01/21/2016	Menyuan, Qinghai	6.4	5.9	dip-slip	10	VIII
10	11/25/2016	Aketao, Xinjiang	6.7	6.6	strike-slip	10	VIII
11	12/08/2016	Hutubi, Xinjiang	6.2	6.0	dip-slip	17	VIII
12	08/08/2017	Jiuzhaigou, Sichuan	7.0	6.5	strike with thrust	20	IX
13	08/09/2017	Jinghe, Xinjiang	6.6	6.3	thrust with slight strike	10	VIII
14	11/18/2017	Milin, Xizang	6.9	6.5	dip-slip	10	VIII
15	06/17/2019	Changning, Sichuan	6.0	5.7	dip-slip	16	VIII
16	01/19/2020	Jiashi, Xinjiang	6.4	6.0	thrust with slight strike	10	VIII
17	05/21/2021	Yangbi, Yunnan	6.4	6.1	strike-slip	10	VIII
18	05/22/2021	Maduo, Qinghai	7.4	7.4	strike-slip	17	X

The M_S and depth values were from CENC, the M_W values were from GCMT, and the I_{max} values were from official websites (see Supplementary Table S1 for details).

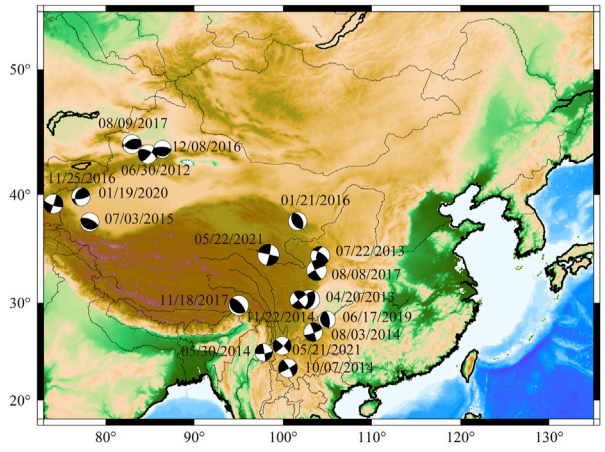

FIGURE 1
Epicenters and focal mechanisms of the 18 studied earthquakes (2012–2021). The epicenter locations were from CENC and the focal mechanism solutions were from GCMT.

To accurately determine the locations of the aftershocks, the HypoDD method (Waldhauser and Ellsworth, 2000) was used to relocate the aftershocks based on the catalog data provided by the CENC. HypoDD accounts for lateral velocity inhomogeneity in the crust, but its effectiveness depends on the velocity structure near the source. Therefore, a subregional *P*-wave velocity model of the crust and upper mantle for each region near the epicenter was considered during the relocation process. The seismic phase data from stations within a range of 200 km–400 km from the epicenter were used for the calculation, depending on the density of local station coverage.

In the following, the definitions of some key parameters are provided.

1. Aftershock ellipse: This refers to the ellipse obtained by fitting the relocated aftershocks using the standard deviational ellipse fitting method.
2. Aftershock center: It represents the geometric center of the aftershock ellipse.
3. Aftershock direction: This term typically denotes the major axis direction of the aftershock ellipse, measured clockwise from the north. The estimated uncertainty is approximately 3%.
4. Aftershock length: It corresponds to the length of the major axis of the aftershock ellipse. The estimated uncertainty is approximately 3%.
5. Macroseismic epicenter: Generally, this refers to the geometric center of the meizoseismal zone, which is the area characterized by the highest intensity levels.
6. Intensity direction: This term denotes the major axis direction of the meizoseismal zone. The estimated uncertainty is approximately 3%.

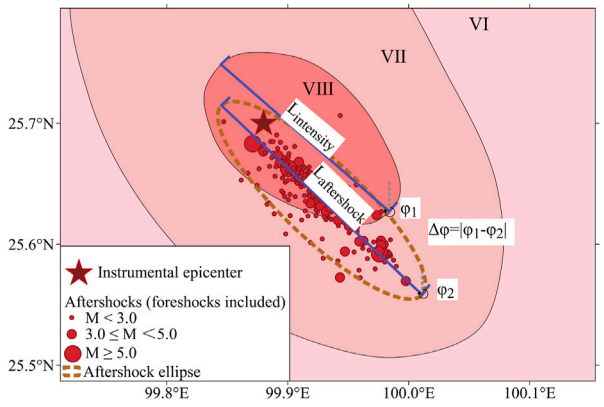

FIGURE 2
The measurement of a sample of the 21 May 2021 M_S 6.4 Yangbi, Yunnan, earthquake.

7. Intensity length: It represents the straight distance between the two farthest points along the intensity contour (typically VIII). The estimated uncertainty is approximately 5%.
8. Difference in direction (°):This refers to the disparity between the aftershock direction and the intensity direction. Figure 2 illustrates an example measurement from the M_S 6.4 Yangbi, Yunnan earthquake that occurred on 21 May 2021. φ_1 and φ_2 represent the intensity direction and the aftershock direction, respectively, while $\Delta\varphi$ indicates the difference in direction. The estimated uncertainty is around 4%.
9. Difference in length (%): it refers to the relative difference between the aftershock length and the intensity length, i.e., $|\frac{L_{aftershock}-L_{intensity}}{L_{larger}}| \times 100\%$, where $L_{aftershock}$ and $L_{intensity}$ are the aftershock length and the intensity length, respectively, as shown in Figure 2, and L_{Larger} is $L_{aftershock}$ or $L_{intensity}$, whichever is larger.

Standard deviational ellipse

Our previous study (Xu et al., 2022) demonstrated the effectiveness of the standard deviational ellipse, also referred to as the directional distribution method, in obtaining an aftershock ellipse. This ellipse is characterized by its center, major and minor axes, and rotation angle (Mitchell, 2005).

The weighted geographic center was calculated as follows:

$$\bar{X}_m = \frac{\sum_{i=1}^{n} m_i x_i}{\sum_{i=1}^{n} m_i} \quad (1)$$

$$\bar{Y}_m = \frac{\sum_{i=1}^{n} m_i y_i}{\sum_{i=1}^{n} m_i} \quad (2)$$

In the given equation, x_i and y_i denote the east-west and north-south coordinate values, respectively, of the ith aftershock. The fitting process involves a total of n aftershocks, with m_i representing the magnitude of the ith aftershock, which is considered as the weighted value in the analysis.

The standard deviations of the major and minor axes of the ellipse were calculated as:

$$\sigma_x = \sqrt{\frac{\sum_{i=1}^{n} \left[\tilde{x}_i \cos\theta + \tilde{y}_i \sin\theta\right]^2}{n}} \quad (3)$$

$$\sigma_y = \sqrt{\frac{\sum_{i=1}^{n} \left[\tilde{x}_i \sin\theta - \tilde{y}_i \cos\theta\right]^2}{n}} \quad (4)$$

where θ was any angle between the x- and the y-axis. $(\tilde{x}_i, \tilde{y}_i)$were the difference between the coordinates (x_i, y_i) of the ith aftershock and the weighted geographic center $((\bar{X}_m, \bar{Y}_m))$, which were calculated by $\tilde{x}_i = x_i - \bar{X}_m$, $\tilde{y}_i = y_i - \bar{Y}_m$. During the calculation, the geographic coordinates were transformed using the Lambert projection.

The rotation angle θ_m of the ellipse represents a specific value, defined as the angle at which the y-axis of the ellipse rotates clockwise from the north, reaching the extreme value of standard

TABLE 2 Parameters of aftershock zones and fault planes of strike-slip earthquakes.

No.	Location	M_S	Fault plane I (strike°/dip°/rake°)#	Fault plane II (strike°/dip°/rake°)#	Difference in directions (°)	Difference in lengths
1	Xinyuan, Xinjiang	6.6	298/60/160	39/73/32	6	54%
2	Yingjiang, Yunnan	6.1	82/79/5	351/85/169	4	35%
3	Ludian, Yunnan	6.5	71/81/-175	340/86/-9	20	0
4	Jinggu, Yunnan	6.6	329/81/174	60/84/9	5	17%
5	Kangding, Sichuan	6.3	143/85/-1	233/89/-175	6	40%
6	Aketao, Xinjiang	6.7	110/78/-177	19/87/-12	0	4%
7	Jiuzhaigou, Sichuan	7.0	151/79/-8	243/82/-168	8	22%
8	Yangbi, Yunnan	6.4	45/80/7	314/83/170	3	19%
9	Maduo, Qinghai	7.4	13/84/-177	283/87/-6	2	4%

#The focal mechanism solutions were from GCMT.

TABLE 3 Parameters of aftershock zones and fault planes of dip-slip earthquakes.

No.	Location	M_S	Fault plane I (strike°/dip°/rake°)#	Fault plane II (strike°/dip°/rake°)#	Difference in directions (°)	Difference in lengths (%)
1	Lushan, Sichuan	7.0	19/49/81	212/42/100	7	28
2	Minxian, Gansu	6.6	196/57/151	303/66/37	14	73
3	Pishan, Xinjiang	6.5	109/22/85	294/68/92	4	28
4	Menyuan, Qinghai	6.4	146/43/83	335/47/96	8	13
5	Hutubi, Xinjiang	6.2	87/22/85	272/68/92	27	16
6	Jinghe, Xinjiang	6.6	101/44/118	244/52/66	26	23
7	Milin, Xizang	6.9	119/24/72	318/67/98	8	21
8	Changning, Sichuan	6.0	350/67/93	162/23/82	5	19
9	Jiashi, Xinjiang	6.4	196/38/31	80/71/124	2	34

#The focal mechanism solutions were from GCMT, except for the Changning earthquake, which was from Xu et al. (2020).

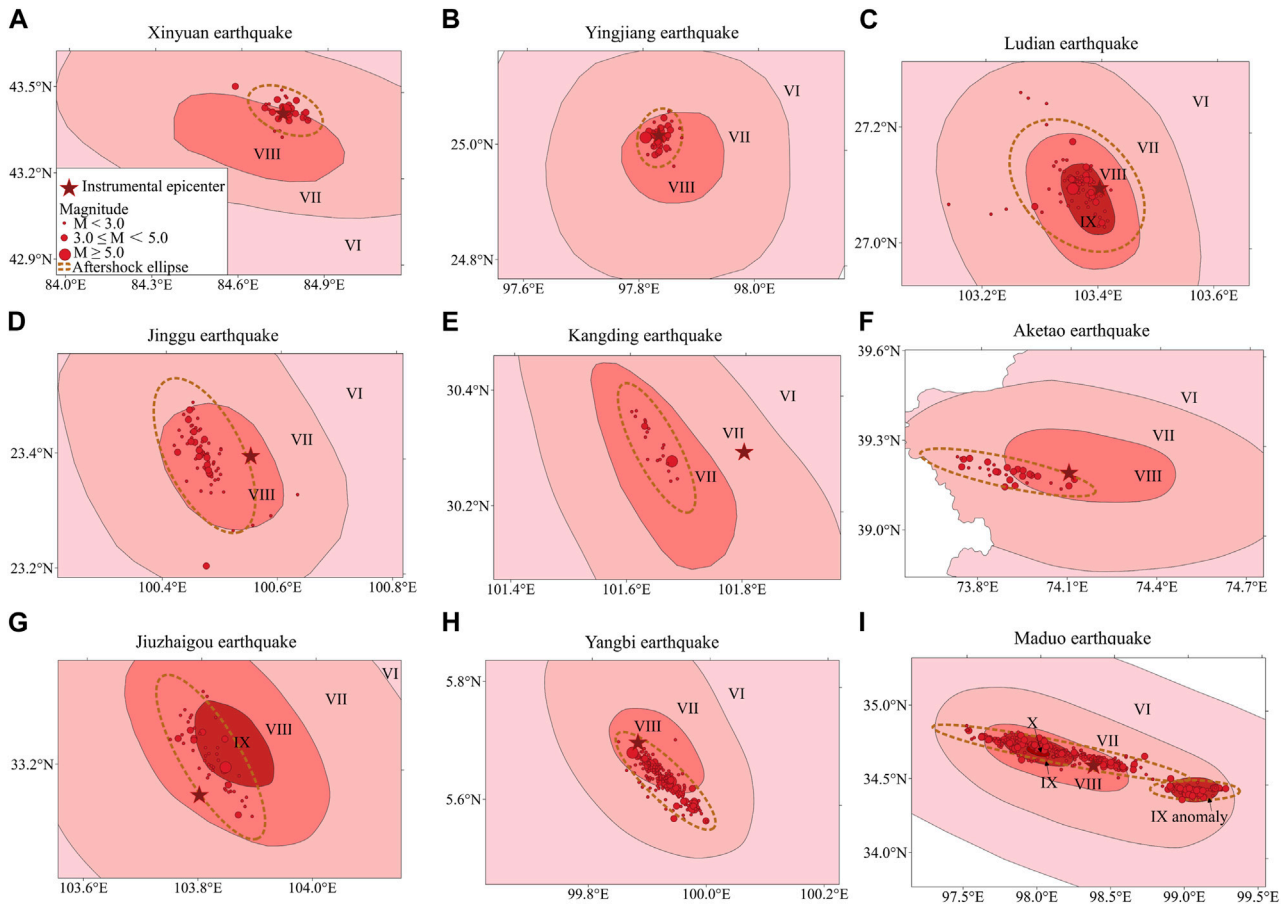

FIGURE 3
The comparison of aftershock ellipses and intensity maps for nine strike-slip earthquakes. **(A)**. The Xinyuan, Xinjiang, earthquake. **(B)**. Yingjiang, Yunnan, earthquake. **(C)**. Ludian, Yunnan, earthquake. **(D)**. Jinggu, Yunnan, earthquake. **(E)**. Kangding, Sichuan, earthquake. **(F)**. Aketao, Xinjiang, earthquake. **(G)**. Jiuzhaigou, Sichuan, earthquake. **(H)**. Yangbi, Yunnan, earthquake. **(I)**. Maduo, Qinghai, earthquake.

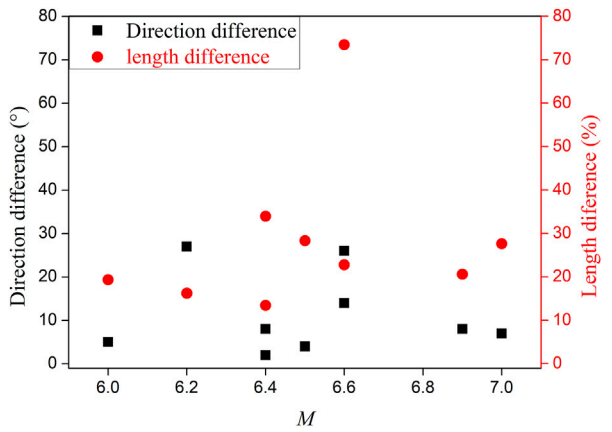

FIGURE 4
The distribution of direction difference and length difference with magnitude for nine strike-slip earthquakes.

deviation along its axis. Lefever (1926) derived Eqs 3, 4 to calculate the standard deviation with respect to θ.

$$\frac{d\sigma}{d\theta} = \frac{\left(\sum_{i=1}^{n}\tilde{y}_i^2 - \sum_{i=1}^{n}\tilde{x}_i^2\right)\cos\theta_m \sin\theta_m + \sum_{i=1}^{n}\tilde{x}_i\tilde{y}_i\left(\cos^2\theta_m - \sin^2\theta_m\right)}{\sqrt{\cos^2\theta_m\sum_{i=1}^{n}\tilde{x}_i^2 + 2\sin\theta_m\cos\theta_m\sum_{i=1}^{n}\tilde{x}_i\tilde{y}_i + \sin^2\theta_m\sum_{i=1}^{n}\tilde{y}_i^2}} = 0 \tag{5}$$

The solution of the above formula was:

$$\theta_m = \arctan\frac{-A + \sqrt{A^2 + 4B^2}}{2B} \tag{6}$$

with

$$A = \sum_{i=1}^{n}\tilde{x}_i^2 - \sum_{i=1}^{n}\tilde{y}_i^2 \tag{7}$$

and

$$B = \sum_{i=1}^{n}\tilde{x}_i\tilde{y}_i \tag{8}$$

The values obtained from Eqs 3, 4, 6–8 can be used to draw the standard deviational ellipse, following the given relation.

$$\left(\frac{x}{\sigma_x}\right)^2 + \left(\frac{y}{\sigma_y}\right)^2 = s \tag{9}$$

where s represented for the confidence value, and a value of 95% was selected in present study.

Results and discussions

The 18 earthquakes analyzed in this study predominantly occurred in the North-South seismic belt and the Tianshan seismic belt within China. They were primarily concentrated in the Xinjiang Uygur Autonomous Region, Yunnan, Sichuan, and Qinghai provinces (Table 1). Yunnan experienced earthquakes solely caused by strike-slip faults, while Sichuan and Qinghai had an equal distribution of strike-slip and dip-slip faults. Other regions primarily consisted of dip-slip faults. Following the relocation process, the average standard errors in longitude, latitude, and vertical directions were reduced to dozens of or a few hundred meters. The average locating residuals were significantly reduced to no more than 0.8 s.

The contours of the aftershock areas exhibited similar shapes to the intensity maps, and all aftershock sequences showed concentrated distribution directions. Considering foreshocks in the analysis did not significantly affect the results, as the results were highly consistent with the analysis that excluded foreshocks. The aftershock lengths measured in this study were found to have minimal dependence on the earthquake's focal mechanism (Supplementary Tables S2, S3), aligning with the findings of Kagan (2002) and Jiang et al. (2007). Table 2 presents the differences in directions for strike-slip earthquakes, and Table 3 displays the results for dip-slip earthquakes.

The variations in directions between the aftershock ellipses and the intensity maps ranged from 0° to 27°, with an average difference of approximately 9°. The differences in lengths between the aftershocks and the intensity maps ranged from 0% to 73%, with an average difference of approximately 25%. In most cases, the lengths of the aftershocks were comparable to intensity levels VIII or VII, except for the M_S 6.6 Xinyuan, Xinjiang earthquake on 30 June 2012, and the M_S 6.6 Minxian, Gansu earthquake on 22 July 2013. The 2-h results for the Xinyuan and Minxian aftershocks aligned

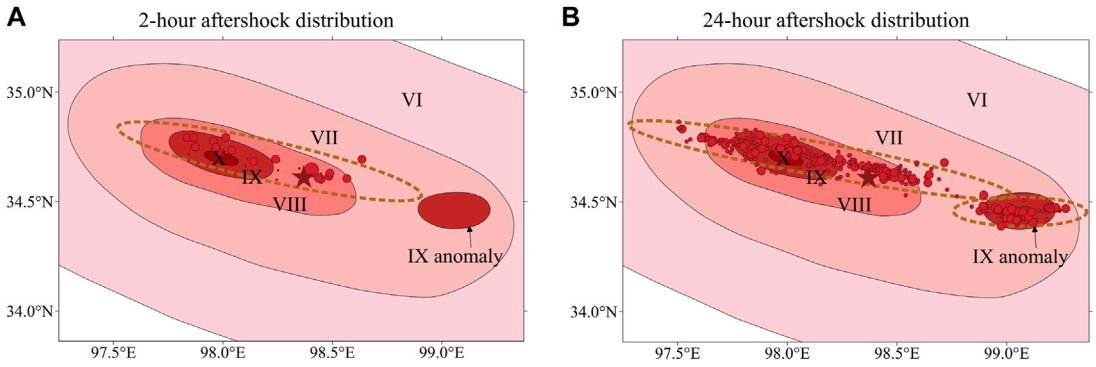

FIGURE 5
The aftershocks within 2 h **(A)** and 24 h **(B)** of the 22 May 2021 M_S 7.4 Maduo, Qinghai, earthquake.

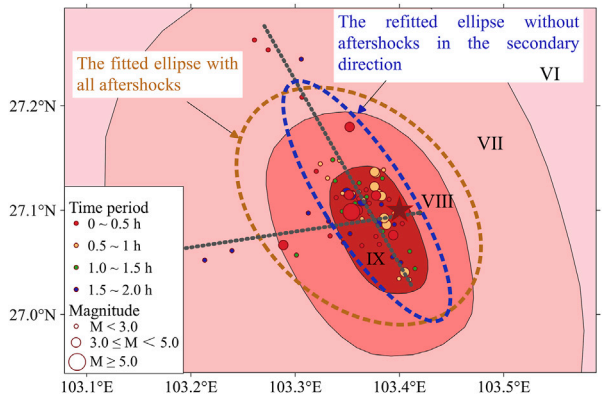

FIGURE 6
The aftershock distribution of the 3 August 2014 M_S 6.5 Ludian, Yunnan, earthquake.

with the aftershocks observed over a longer time frame, which were concentrated in small areas. Apart from these two cases, the differences between aftershock lengths and intensity lengths varied from 0% to 40%, with an average difference of approximately 20%. The discrepancy between the macroseismic epicenter and the aftershock center did not show significant improvement when compared to the difference between the instrumental and macroseismic epicenters.

Comparison of aftershock areas with intensity maps for strike-slip earthquakes

Figures 3A–I presents the results of the aftershock ellipses and macroseismic intensity maps for nine strike-slip earthquakes. It can be observed that most of the aftershock ellipses align with the VIII contours. Some discrepancies in the Figure 3 between aftershock position and isoseismal area could be due to differences in the number of inhabitants, especially for the earthquakes happened in the Xinjiang Uygur Autonomous Region (Figures 3A, F), since the macroseismic intensity maps obtained from field surveys were mainly based on the damage to the houses. The values for direction difference and length difference are provided in Table 2 and illustrated in Figure 4. The differences in directions are predominantly below 10°, with an average of 6°. It is worth noting that a direction difference of 30° is acceptable for quick

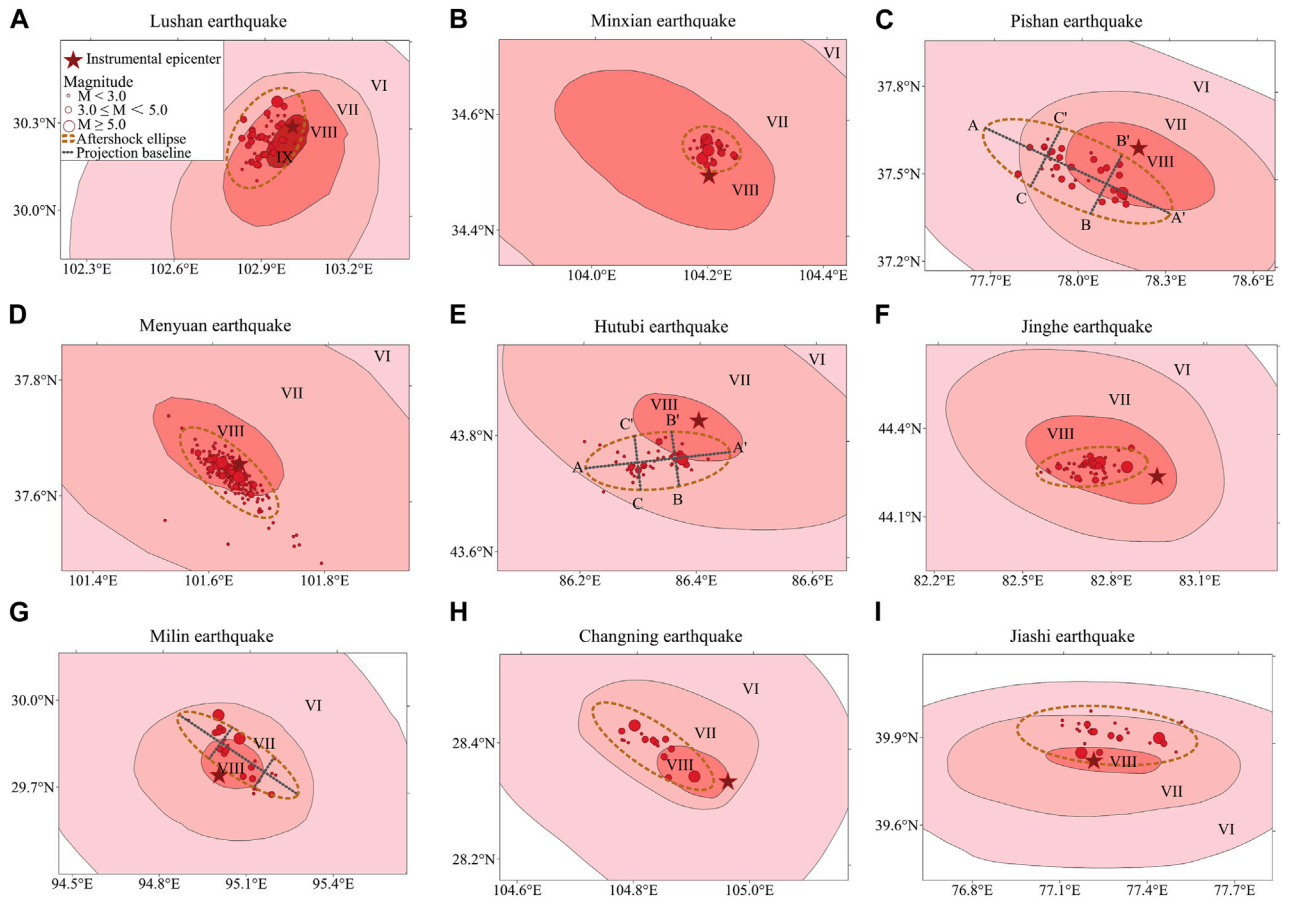

FIGURE 7
The comparison of aftershock ellipses and intensity maps for nine dip-slip earthquakes. For the Pishan and the Hutubi earthquakes, AA′ indicates the aftershock direction, while BB′ and CC′ directions are perpendicular to the aftershock direction. **(A)**. The Lushan, Sichuan, earthquake. **(B)**. Minxian, Gansu, earthquake. **(C)**. Pishan, Xinjiang, earthquake. **(D)**. Menyuan, Qinghai, earthquake. **(E)**. Hutubi, Xinjiang, earthquake. **(F)**. Jinghe, Xinjiang, earthquake. **(G)**. Milin, Xizang, earthquake. **(H)**. Changning, Sichuan, earthquake. **(I)**. Jiashi, Xinjiang, earthquake.

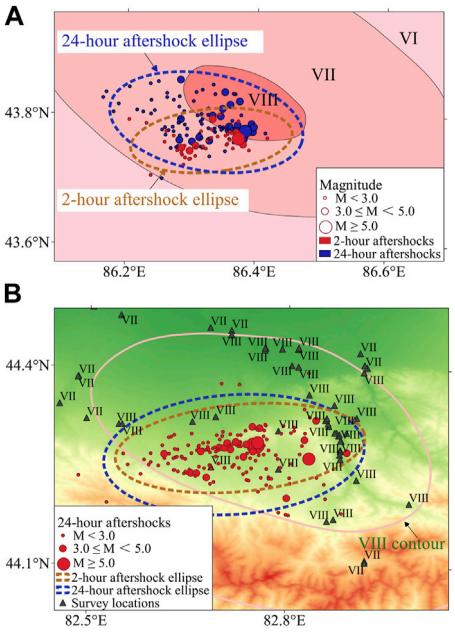

FIGURE 8
(A) The aftershocks within 2 and 24 h of the Hutubi earthquake. **(B)** The aftershocks within 24 h and the field survey locations and intensity values of the Jinghe earthquake.

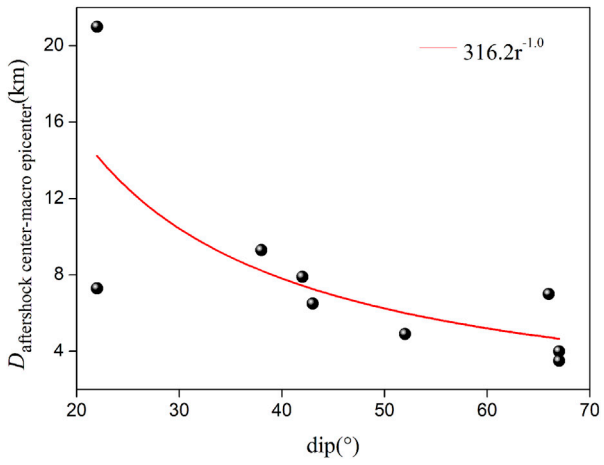

FIGURE 9
The distribution of the distance between the aftershock center and the macroseismic epicenter with dip.

assessment shortly after an earthquake. Consequently, the aftershock direction proves to be useful in assessing the intensity direction. Furthermore, there seems to be no significant relationship between the direction difference and length difference with the magnitude of the earthquake (Figure 4).

For most of the studied earthquakes, the maximum intensity reached VIII, with a few cases reaching IX, and the M_S 7.4 Maduo, Qinghai earthquake on 22 May 2021, reaching X. Additionally, there was an anomaly of intensity IX in the southeast region of the meizoseismal zone of the Maduo earthquake (Figure 5). The majority of the relocated locations within the 2-h timeframe were situated within the epicentral zones, which are approximately 60 km wide (Figure 5A). However, there were two distinct clusters in the distribution of the 24-h aftershocks (Figure 5B). This 24-h aftershock distribution precisely corresponds to the intensity map. Although with fewer aftershocks, the direction of the aftershocks within a 2-h period aligns with that observed over 24 h. The aftershock length within 2 h (131.4 km) matches the combined lengths of the VIII and IX anomaly (126.0 km, see Supplementary Table SA2), with a difference of 4%.

The maximum difference in direction is 20°, observed in the M_S 6.5 Ludian, Yunnan earthquake on 3 August 2014. The relocated aftershock distribution of this earthquake displays a primary direction of NW and a secondary direction of approximately EW (Figures 3C, 6), which is not uncommon for strike-slip earthquakes. When the aftershocks in the secondary direction were excluded from the fitting data, a new aftershock ellipse was obtained (Figure 6). The difference between the new aftershock direction and the VIII direction was reduced to 7°. Based on this, it is suggested to obtain the aftershock ellipse by excluding the aftershocks in the minor direction and considering the aftershock direction as the assessed intensity direction. Additionally, both the original and refitted aftershock lengths of the Ludian earthquake show perfect agreement with the length of intensity VIII.

Table 2 reveals that the strikes of the two fault planes for strike-slip earthquakes exhibit a difference of nearly 90° or 270°. Xu et al. (2022) highlighted that one of the fault plane strikes from the focal mechanism was notably consistent with the intensity direction in over 83% of earthquakes in Chinese mainland. Therefore, the seismogenic fault can be determined based on the relocated aftershock direction. For example, the fault plane parameters for the Maduo earthquake were 13°/84°/-177° (fault plane I) and 283°/87°/-6° (fault plane II), respectively. The measurement of the aftershock direction resulted in a value of 103°, aligning with 283° in a straight line (Supplementary Table S2). Hence, fault plane II with a strike of 283° was identified as the seismogenic fault.

Comparison of aftershock areas with intensity maps for dip-slip earthquakes

All the dip-slip earthquakes examined in this study were attributed to thrust faults. Comparing the aftershock ellipses with the intensity maps (Figures 7A–I), it is evident that the aftershock directions align well with the intensity directions, with an average difference of 11°. Similar to the findings for the strike-slip earthquakes, it can be concluded that the aftershock direction is valuable for assessing the intensity direction during rapid assessments.

As depicted in Figure 7, the lengths of the aftershocks generally correspond to the intensity lengths, except for the Minxian earthquake (Figure 7B), where the aftershock distribution was highly concentrated in a small area. In most cases, the lengths associated with intensity VIII are recommended for comparison with the aftershock lengths. However, intensity VII is preferred for the Milin earthquake (Figure 7G) and the Changning earthquake

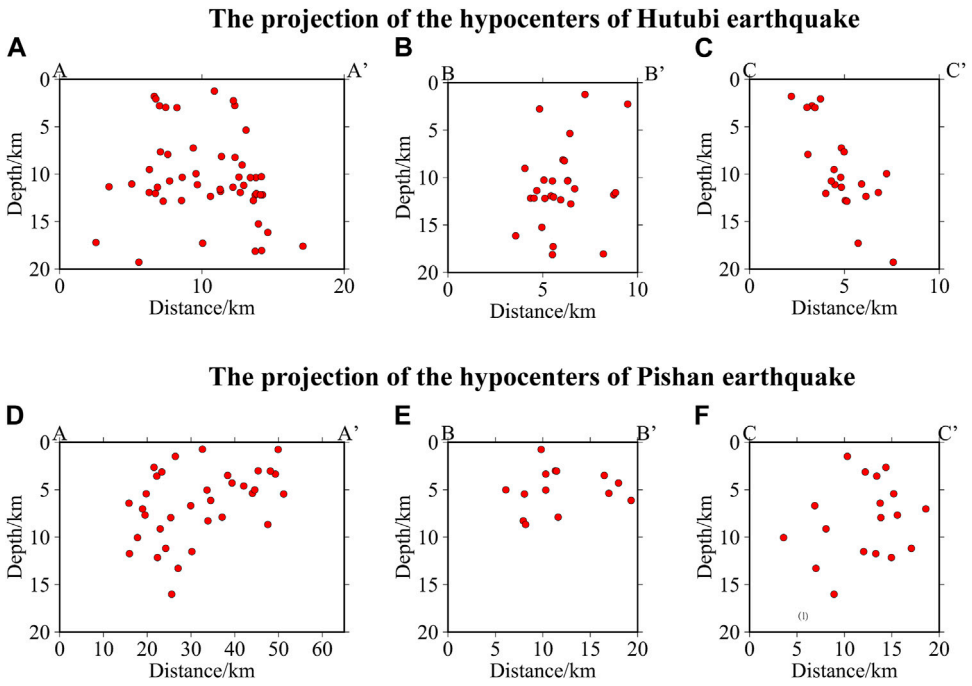

FIGURE 10
The projections of the hypocenters onto vertical planes along and perpendicular to the aftershock directions for the Hutubi earthquake **(A–C)** and the Pishan earthquake **(D–F)**. The projection width for each case depended on the distribution area of the aftershocks.

(Figure 7H). This discrepancy can be attributed, in part, to the uninhabited VIII zone in the former case, which was only one-seventh the size of the VII area, while the latter earthquake had a relatively shallow focal depth, resulting in an VIII area of only 84 km^2 (Xu et al., 2020). It is understandable that the highly affected intensities in these two earthquakes are 1 unit lower than the others. The majority of the length differences between the aftershocks and the intensities (VII for the Milin and Changning earthquakes, and VIII for the others) are within 30%, except for the Minxian earthquake. Hence, the aftershock length serves as a reference for assessing the intensity length.

The direction differences for the Hutubi earthquake (Figure 7E) and the Jinghe earthquake (Figure 7F) are not as favorable as the others, with direction differences of 27° and 26°, respectively (Table 3). The 24-h aftershocks for these two earthquakes were also analyzed, and the results are illustrated in Figure 8. The 24-h results for the Hutubi earthquake align better with the VIII direction, reducing the difference to 12° (Figure 8A). It is presumed that the earlier aftershocks occurred on a secondary fault, while the later aftershocks occurred on the main fault. Therefore, a dynamic correction of the intensity direction based on aftershocks during different time periods is suggested for earthquakes with complex seismogenic causes, such as the Hutubi earthquake.

Figure 8B illustrates that the 24-h aftershock direction of the Jinghe earthquake generally aligns with the 2-h result, with a difference consistently above 20°. It is apparent that the southern part of the VIII contour had a lack of survey locations due to its high altitude. Therefore, the major axis direction of the VIII contour was inferred based on topography and geological structure during the field survey. However, from a seismological perspective, it is more appropriate to infer the major axis direction based on the aftershock direction. This suggests the importance of considering the aftershock distribution along with other factors during seismic intensity surveys.

There exists a certain disparity between the macroseismic epicenter and the aftershock center, partly attributed to the presence of dip and the rupture mode (unilateral for the Changning earthquake and asymmetric bilateral rupturing for the Lushan earthquake). In the case of dip-slip earthquakes, the aftershocks and high intensities predominantly occur on one side of the seismic faults (Figure 7), and the distance between the aftershock center and the macroseismic epicenter increases as the dip decreases (Figure 9). A power function fitting yields $D = 316.2 \times r^{-1.0}$, where r represents the dip. This indicates that the aftershock center and the macroseismic epicenter become closer as the dip angle increases. However, further study is required to refine the fitting using additional earthquake parameters.

The strikes of the two fault planes for the nine thrust faults exhibit differences ranging from 110° to 200°, as shown in Table 3. In cases where the strike difference is approximately 180°, it is nearly impossible to determine the seismogenic fault based solely on the epicenter distribution of aftershocks. For earthquakes with two distinct dip angles, such as the Hutubi (Figure 7E) and Pishan (Figure 7C) earthquakes, the spatial distributions of aftershocks were taken into consideration, as presented in Figure 10. The projection lines are marked in Figure 7.

Figure 10 demonstrates the vertical plane projections of the hypocenters, revealing a steep slope for the Hutubi earthquake (Figures 10A–C) and a gentle slope for the Pishan earthquake

(Figures 10D–F). Consequently, the assumed seismogenic fault parameters for the Hutubi earthquake were 272°/68°/92°, while for the Pishan earthquake, they were 109°/22°/85° (Table 3). According to the definition of the focal mechanism solution, the dip is on the right-hand side along the strike, confirming the presence of hanging wall and footwall for these two earthquakes. Taking the hanging wall effect into consideration, an estimation of the approximate location of the macroseismic epicenter can be made by shifting the aftershock center to the hanging wall. The extent of this shift requires further research to refine the relationship between the difference in location and the dip (Figure 9).

In summary, the intensity direction, VIII length, and the location of the macroseismic epicenter are approximately determined based on the findings discussed above, providing a foundation for rapid intensity assessment. These conclusions reaffirm the importance of considering aftershocks in rapid assessment and emergency response efforts following large earthquakes.

Conclusion

This study focuses on 18 aftershock-rich earthquakes ($M_S \geq 6.0$) that occurred in Chinese mainland over the past decade. The relocation of aftershock hypocenters was carried out using the hypoDD method, while the standard deviational ellipse was employed to determine the aftershock ellipses. The key conclusions derived from this analysis are as follows.

(1) The aftershock directions and lengths generally align with the intensity maps. The average difference in direction is approximately 9° for all 18 earthquakes, and the average length difference is around 20% for 16 earthquakes, excluding the Xinyuan and Minxian earthquakes, where the aftershocks were concentrated in small areas. Discrepancies between the aftershock positions and the isoseismal areas could be attributed to variations in population density. Consequently, the 2-h aftershock distribution provides valuable information for determining the direction and VIII length of the assessed intensity map.

(2) Aftershock distribution aids in identifying the seismogenic fault. For earthquakes primarily associated with strike-slip faults, the two strikes provided by the focal mechanism solution typically differ by approximately 90° or 270°. The nodal plane with a strike close to the aftershock direction is inferred to be the seismogenic fault plane. In the case of the Ludian earthquake, the aftershocks exhibit one major direction and one minor direction. It is suggested to exclude the aftershocks in the minor direction when constructing the aftershock ellipse, and the resulting aftershock direction can be considered as the assessed intensity direction.

(3) In earthquakes predominantly related to thrust faults where the two strikes provided by the focal mechanism solution differ by approximately 180°, determining the seismogenic fault based solely on the epicenter distribution of aftershocks is insufficient. Therefore, the aftershocks were projected onto vertical planes along and perpendicular to the aftershock direction. For earthquakes exhibiting distinct dip angles, this projection enables the determination of the dip and differentiation between the seismogenic fault and the auxiliary plane. Moreover, the distance between the aftershock center and the macroseismic epicenter increases as the dip decreases. A preliminary fitting suggests a relationship of $D = 316.2 \times r^{-1.0}$, where r represents the dip. Further optimization of this fitting is needed to enhance accuracy. The approximate location of the macroseismic epicenter can be estimated by shifting the aftershock center to the hanging wall using a refined fitting relation.

(4) In some cases, the 2-h aftershocks occurred on a secondary fault, while subsequent long-term aftershocks occurred on the main fault, as observed in the Hutubi earthquake. To improve the assessment of the intensity map, a dynamic correction of the intensity direction based on aftershocks during different periods is suggested. Additionally, uneven distribution of survey locations around the epicenter due to topographical factors, such as in the Jinghe earthquake, calls for inferring the major axis direction of the intensity map based on the aftershock direction from a seismological standpoint.

To summarize, China is prone to seismic activity, and it is highly probable that large earthquakes will impact Chinese mainland in the future. The findings of this study have important implications for the rapid assessment of intensity maps following such events. It is important to highlight the significant advancements made in instrumental intensity determination and earthquake early warning systems in recent years within Chinese mainland. These advancements enable quick assessments of seismic hazards. Therefore, one of the key challenges in the field of macroseismology in Chinese mainland is to establish the relationship between traditional intensity maps and instrumental intensity values. Further research is necessary to comprehensively evaluate the intensity distribution of large earthquakes in a comprehensive manner.

Data availability statement

The original contributions presented in the study are included in the article/Supplementary Material, further inquiries can be directed to the corresponding author.

Author contributions

ZX and JL conceptualized the study idea and wrote the original draft. AY prepared Figures 1–6 and XL prepared Figures 7–10. JR and XW prepared Tables 1–3. All authors contributed to the article and approved the submitted version.

Funding

This work was supported by the National Key Research and Development Program of China (Grant No. 2018YFC1504006) and the Spark Program of Earthquake Sciences (Grant No. XH20071Y).

Conflict of interest

The authors declare that the research was conducted in the absence of any commercial or financial relationships that could be construed as a potential conflict of interest.

Publisher's note

All claims expressed in this article are solely those of the authors and do not necessarily represent those of their affiliated organizations, or those of the publisher, the editors and the reviewers. Any product that may be evaluated in this article, or claim that may be made by its manufacturer, is not guaranteed or endorsed by the publisher.

Supplementary material

The Supplementary Material for this article can be found online at: https://www.frontiersin.org/articles/10.3389/feart.2023.1128827/full#supplementary-material

References

Allen, T. I., Wald, D. J., and Worden, C. B. (2012). Intensity attenuation for active crustal regions. J. Seismology*16* 16, 409–433. doi:10.1007/s10950–012–9278–7

Astiz, L., Shearer, P. M., and Agnew, D. C. (2000). Precise relocations and stress change calculations for the Upland earthquake sequence in southern California. *J. Geophys. Res.* 105, 2937–2953. doi:10.1029/1999jb900336

Bakun, W. H., and Scotti, O. (2006). Regional intensity attenuation models for France and the estimation of magnitude and location of historical earthquakes. *Geophys. J. Int.* 164, 596–610. doi:10.1111/j.1365-246x.2005.02808.x

Cai, G., Wang, W., Wu, J., Su, J., Lai, G., Wu., P., et al. (2023). Three-dimensional body wave velocity structure and seismogenic structure for the 2022M_S6.8 Luding earthquake sequence in Sichuan, China. *Front. Earth Sci.* 11, 1114. doi:10.3389/feart.2023.1099744

Chen, K., Yu, Y., Gao, M., and Kang, C. (2018). Comparative study on ShakeMaps of PGA for the napa M_W6 0 earthquake on 24 aug. 2014 constrained by different conditions, *Seismol. Geol* 40, 440–449. doi:10.3969/j.issn.0253-4967.2018.02.011

Cilia, M. G., Mooney, W. D., and Robinson, A. (2017). A seismic intensity survey of the 1 april 2014 *M* 8 2 iquique, Chile, earthquake and tsunami, and a comparison with strong-motion data. *Seismol. Res. Lett.* 88, 1232–1240. doi:10.1785/0220170030

Dziewonski, A. M., Chou, T.-A., and Woodhouse, J. H. (1981). Determination of earthquake source parameters from waveform data for studies of global and regional seismicity. *J. Geophys. Res.* 86, 2825–2852. doi:10.1029/JB086iB04p02825

Ekström, G., Nettles, M., and Dziewonski, A. M. (2012). The global CMT project 2004 T010: Centroid-moment tensors for 13017 earthquakes. *Phys. Earth. Planet. Inter.* 2000y01, 11y. doi:10.1016/j.pepi.2012.04.002

Ferrario, M. F., Livio, F., Capizzano, S. S., and Michetti, A. M. (2020). Developing the first intensity prediction equation based on the environmental scale intensity: A case study from strong normal-faulting earthquakes in the Italian apennines. *Seismol. Res. Lett.* 91, 2611–2623. doi:10.1785/0220200044

Galli, P., Castenetto, S., and Peronace, E. (2017). The macroseismic intensity distribution of the 30 October 2016 earthquake in central Italy (M_W 6.6): Seismotectonic implications. *Tect.* 36, 2179–2191. doi:10.1002/2017TC004583

Henry, C., and Das, S. (2001). Aftershock zones of large shallow earthquakes: Fault dimensions, aftershock area expansion and scaling relations. *Geophys. J. Int.* 147, 272–293. doi:10.1046/j.1365-246x.2001.00522.x

Jiang, H. K., Zheng, J. C., Wu., Q., Qu, Y. J., Li, Y. L., and Dai, L. (2007). Statistical features of aftershock distribution size for moderate and large earthquakes in Chinese mainland. *Acta Seismol. Sin.* 29, 151–164. (in Chinese with English abstract). doi:10.1007/s11589-007-0158-0

Kagan, Y. Y. (2002). Aftershock zone scaling. *Bull. Seismol. Soc. Am.* 92, 641–655. doi:10.1785/0120010172

Kiani, A., Torabi, M., and Mirhosseini, S. M. (2019). Intensity measures for the seismic response evaluation of buried steel pipelines under near-field pulse-like ground motions. *Earthq Eng Eng Vib* 18, 917. doi:10.1007/s11803–019–0543–4

Kisslinger, C., and Jones, L. M. (1991). Properties of aftershock sequences in southern California. *J. Geophys. Res.* 96, 11947–11958. doi:10.1029/91JB01200

Lefever, D. W. (1926). Measuring geographic concentration by means of the standard deviational ellipse. *Am. J. Soc.* 32, 88–94. doi:10.1086/214027

Lekkas, E. L. (2010). The 12 may 2008 M_W 7.9 wenchuan, China, earthquake: Macroseismic intensity assessment using the EMS-98 and ESI 2007 scales and their correlation with the geological structure. *Bull. Seismol. Soc. Am.* 100, 2791–2804. doi:10.1785/0120090244

Li, Y., and Pu, W. (2022). Analyzing the 2020 M-w 6.4 Puerto Rico earthquake sequence based on the epidemic-type aftershock sequence model. *Seismol. Res.Lett.* 93, 609–619. doi:10.1785/0220210217

Matumoto, T., and Latham, G. (1973). Aftershocks and intensity of the managua earthquake of 23 december 1972,*Science* 181, 5455447.doi:10.1785/0220210217

Mitchell, A. (2005). *The esri guide to GIS analysis spatial measurement & statistics*. California: Esri Press, 49–50.

Neo, J. C., Huang, Y., Yao, D., and Wei, S. (2020). Is the aftershock zone area a good proxy for the mainshock rupture area? *Bull. Seismol. Soc. Am.* 111, 424–438. Se. doi:10.1785/0120190200

Sun, B., Yan, P., and Chen, X. (2014). New characteristics of intensity assessment of sichuan lushan "4.20" *Ms*7.0 earthquake. *Earthq. Eng.& Eng. Vib.* 13, 123–139. doi:10.1007/s11803-014-0243-z

Tesfamariam, S., and Goda, K. (2022). Risk assessment of CLT-RC hybrid building: Consideration of earthquake types and aftershocks for Vancouver, British Columbia. *Soil Dyn. Earthq. Eng.* 156, 107240–111102. doi:10.1016/j.soildyn.2022.107240

Vannucci, G., Lolli, B., and Gasperini, P. (2021). Inhomogeneity of macroseismic intensities in Italy and consequences for macroseismic magnitude estimation. *Seismol. Res.Lett.* 92, 2234–2244. doi:10.1785/0220200273

Waldhauser, F., and Ellsworth, W. (2000). A double-difference earthquake location algorithm: Method and application to the Northern Hayward Fault, California. *Bull. Seismol. Soc. Am.* 90, 1353–1368. doi:10.1785/0120000006

Wang, D., Xie, L. L., and Abrahamson, N. A. (2010). Comparison of strong ground motion from the wenchuan, China, earthquake of 12 may 2008 with the next generation attenuation (NGA) ground-motion models. *Bull. Seismol. Soc. Am.* 100, 2381–2395. doi:10.1785/0120090009

Wang, S., Yu, Y., Gao, A., and Yan, X. (2000). Development of attenuation relations for ground motion in China. *Earth. Res. China* 16, 996r06. (in Chinese with English abstract).

Xu, Z. S., Liu, J., Zheng, T. Z., Ren, J., Chen, Y. H., and Li, X. L. (2020). Isoseismal line of Sichuan Changning M_S6.0 earthquake in 2019 based on precisely located aftershocks sequence. *Acta Seismol. Sin.* 42, 4474456. (in Chinese with English abstract). doi:10.11939/jass.20200072

Xu, Z. S., Ren, J., Tan, Z. T., Gao, X. Y., Chen, Y. H., Yang, Z. G., et al. (2022). Determination of the long-axis direction of the seismic influence field using the strike of the focal mechanism solution. *J. Seismo. Res.* 45, 88–99. doi:10.20015/j.cnki.ISSN1000–0666

Yuan, Y. (2008). Impact of intensity and loss assessment following the great wenchuan earthquake. *Earthq. Eng. Eng. Vib.* 7, 247–254. doi:10.1007/s11803-008-0893-9

Zhang, Y., Zhi, X., and Fan, F (2019). Study of the correlations between main shocks and aftershocks and aftershock synthesis method. *Earthq. Eng. Eng. Vib.* 18, 759–775. doi:10.1007/s11803–019–0535–4